ETH
Eidgenössische Technische Hochschule Zürich
Swiss Federal Institute of Technology Zurich

Seminar for Applied Mathematics SAM

Electromagnetic Near-Field based Pose Estimation for Autonomous Systems

H. Gietler and H. Ammari and H. Zangl

Research Report No. 2019-29

June 2019
Latest revision: June 2019

Seminar für Angewandte Mathematik
Eidgenössische Technische Hochschule
CH-8092 Zürich
Switzerland

Funding SNF: 200021--172483

Electromagnetic Near-Field based Pose Estimation for Autonomous Systems

Harald Gietler, Habib Ammari, and Hubert Zangl

Abstract

Under certain circumstances delicate maneuvers in the robotics field, such as autonomous landing of unmanned aerial vehicles or calibration of robot arms, let state-of-the-art pose estimation concepts face their limits. In GPS denied environments most current state estimation approaches are based on visual-inertial odometry, which suffer from random drift, motion blur and low overlap between consecutive images. A wire-less electromagnetic field-based sensor system is proposed which enables tracking of moving objects e.g. drones. The gathered up to 6-degrees of freedom information is complementary to existing sensing principles e.g. GPS or vision-based systems. Additionally, it can be used for stand-alone navigation or non-invasive localization of medical devices inside the human body. The sensor system is comprised of an exciter and a sensor. The exciter can be mounted on a moving robot and generates an electromagnetic field. The field is measured by the sensor and subsequently, the pose of the exciter with respect to the sensors' pose is estimated. Conductive objects in the vicinity of the sensor alter the measured magnetic field due to induced eddy currents. In general, unmanned aerial vehicles or wheeled robots mainly consist of conductive materials, which causes a significant estimation error. A low-complexity method to suppress the influence of those objects is introduced. The approach is verified using a Finite Element based solution of the full Maxwell's equations. Due to the computational savings, the methodology can be used in real-time pose estimation schemes, which is showcased using an Extended Kalman Filter.

Index Terms

Computational electromagnetics, Eddy currents , Magnetic field measurement, Pose estimation , Kalman filters.

H. Gietler and H. Zangl are with the Institute of Smart Systems Technologies at the University of Klagenfurt, Klagenfurt, Austria, e-mail: harald.gietler@aau.at

H. Ammari is with the Department of Mathematics at the Swiss Federal Institute of Technology in Zurich, ETHZ, Zurich, Switzerland

I. INTRODUCTION

Along with the growing number of autonomous mobile platforms, the demand of accurate localization approaches for navigational tasks increases. Recent research focuses on indoor navigation, a global positioning system (GPS)-denied environment, using visual and inertial sensors for pose estimation [1]. However, their accuracy decreases when approaching objects. Reasons are, e.g. motion blur and low overlap between consecutive images. Alternatively, ultra wide band (UWB) modules have been used for indoor localization enabling high accuracy [2] and the capability of data transmission at the same time. However, a direct line of sight is necessary between transmitter and receiver to maintain accuracy [3], [4]. This issue is addressed by placing redundant UWB modules, which increases the chance to cover the targeted object. Alternatively, electromagnetic field based sensors can be used to estimate the pose of the mobile platform [5], [6]. Recently magnetic field based sensors were proposed as non-invasive localization method for miniature medical device in human bodies [7]. Electromagnetic field based approaches do not rely on direct line-of-sight and do not drift over time. The drawback is the limited range, but usually the accuracy increases with decreasing distance. Thus, they are beneficial for the robotics field [8], [9] especially when using them complementary to existing systems such as visual-inertial odometry (VIO). This paper introduces a robust electromagnetic field based localization concept. It is comprised of an electromagnetic field emitter and a magnetic field sensor. The emitter can be positioned on any moving platform, e.g. robot arm end effector or a unmanned aerial vehicle (UAV). The sensor is supposed to have a fixed pose and its measurement data is used to estimate the relative pose of the field source. It is well known, that conductive materials in the vicinity of the field alter the field distribution. This is caused by induced eddy currents which create an additional electromagnetic field which interacts with the original field. The introduced concept is able to suppress the influence of known conductive materials such as the moving platform itself. This significantly increases the robustness of the approach especially for highly conductive materials, e.g. metals. Note, that iterative solving of the Maxwell's equations is avoided. In contrast, it is based on an explicit field formulation [10]. The accuracy of the formulation is verified by comparing it to a classical Finite Element Method (FEM) based solution. Due to its low computational complexity the concept is especially useful for real-time applications. This is ultimately showcased by using an Extended Kalman Filter (EKF) based tracking approach.

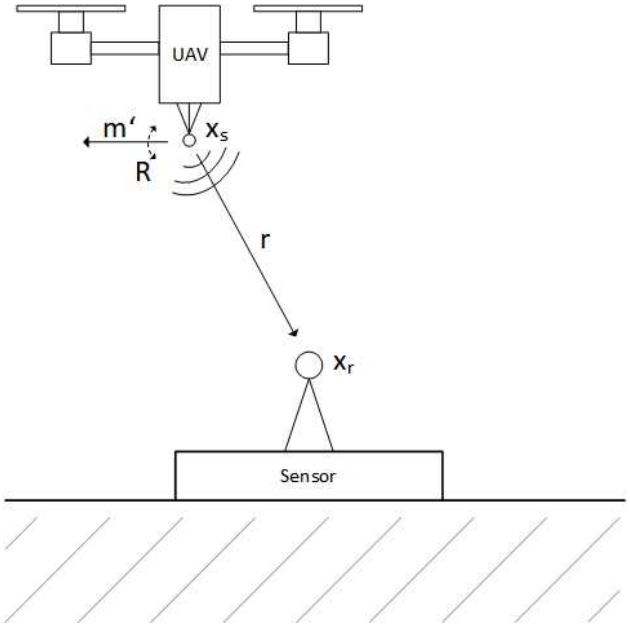

Fig. 1. A schematic view of the proposed system. The electromagnetic field emitter is mounted on the mobile platform, i.e. UAV, whereas the sensor is attached to the ground. The relative position and orientation of and emitter are of interest.

II. System Model

The proposed concept consists of a freely movable alternating magnetic field source (emitter) e.g. attached to a UAV, and a magnetic field sensor arrangement with a fixed position and attitude, e.g. on the ground. Ideally, the emitter consists of three point dipole sources with orthogonal magnetic dipole moments. A manufacturable system could be a stack of small orthogonally placed coils, which can be approximated by a dipole model. The approximation is valid in certain limits described in [11]. Alternatively, each coil can be modelled as a stack of magnetic point sources rather than just multiplying the magnetic dipole moment with the number of turns. Such a coil structure may efficiently be driven using rectangular waveforms and employing parallel resonant circuitries. The complementary magnetic field sensor could also consist of three orthogonally placed pick-up coils to serve for all three spatial axis.

The first analysis neglects the emitter carrying platform and the surrounding space is assumed to be air. The magnetic field strength at the sensor position $\mathbf{x}_r$ is then given by [12]

$$\mathbf{H}_0(\mathbf{r},\mathbf{m}) = \begin{bmatrix} H_x \\ H_y \\ H_z \end{bmatrix} = \frac{1}{4\pi}\left(\frac{3\mathbf{r}(\mathbf{m}\cdot\mathbf{r})}{|\mathbf{r}|^5} - \frac{\mathbf{m}}{|\mathbf{r}|^3}\right). \tag{1}$$

The quantities $\mathbf{r} = \mathbf{x}_r - \mathbf{x}_s$, $\mathbf{m}$ and μ_0 denote the relative position with respect to the emitter, the magnetic moment of the emitter and the permeability of free space, respectively. An understandable visualization of the geometrical dependencies is shown in Fig. 1. If the attitude of the mobile platform changes, $\mathbf{r}$ remains the same whereas $\mathbf{m}$ would be altered. Therefore, the magnetic dipole moment can be utilized to model the attitude of the emitter and more generic the attitude of the mobile platform. Reformulating the magnetic dipole moment yields

$$\mathbf{m} = \mathbf{R}\mathbf{m}' \ , \tag{2}$$

where $\mathbf{m}'$ is the magnetic dipole moment in initial situation and $\mathbf{R} \in \mathbb{R}^{3\times3}$ is a rotational matrix with $\mathbf{x}_s$ being the center of rotation. $\mathbf{R}$ is defined by the rotation angles $\boldsymbol{\theta} \in \mathbb{R}^3$ and the rotation sequence

$$\mathbf{R} = \mathbf{R}_z\mathbf{R}_y\mathbf{R}_x, \tag{3}$$

where $\mathbf{R}_z$, $\mathbf{R}_y$ and $\mathbf{R}_x$ are given by

$$\mathbf{R}_z = \begin{bmatrix} \cos\theta_3 & -\sin\theta_3 & 0 \\ \sin\theta_3 & \cos\theta_3 & 0 \\ 0 & 0 & 1 \end{bmatrix}, \ \mathbf{R}_y = \begin{bmatrix} \cos\theta_2 & 0 & \sin\theta_2 \\ 0 & 1 & 0 \\ -\sin\theta_2 & 0 & \cos\theta_2 \end{bmatrix}, \ \mathbf{R}_x = \begin{bmatrix} 1 & 0 & 0 \\ 0 & \cos\theta_1 & -\sin\theta_1 \\ 0 & \sin\theta_1 & \cos\theta_1 \end{bmatrix}. \tag{4}$$

Suppose, the magnitude of the magnetic moment is known, then the magnetic field strength at any observation point is described by 6-degrees of freedom (DOF), i.e. the space vector pointing from the emitter to the point of observation and the attitude of the emitter. For some applications partial information about the pose already exists which can be used to reduce the model complexity.

Independent of the field model, different kind of magnetic sensors can be used to measure the local magnetic field. A common way to measure alternating magnetic fields are pick-up coils [13], [14]. Faraday's Law links the local magnetic field strength to the induced electromagnetic force. For a homogeneous magnetic field in the cross section of a air-cored solenoid the electromagnetic force is approximately given by [15]

$$V = -\mu_0 N\mathbf{A}\cdot\frac{\delta\mathbf{H}}{\delta t}, \tag{5}$$

where N is the number of windings and $\mathbf{A}$ represents the area of the cross section of the coil. For a non-homogeneous magnetic field, e.g. dipole field, this can still be a good approximation depending on the location of the point of observation. The taken measurements are the basis for the pose estimation. Due to the model order a single observation is not sufficient to get an accurate estimate. Therefore, a number of either sensors or emitters is required.

III. Tracking of a Mobile Target

This sections presents an approach to estimate both the location and the orientation of the target. A widely used approach to track system states is the Kalman Filter (KF). It produces an optimal estimator for linear systems with Gaussian noise. The EKF is the generalization of the KF to non-linear dynamical systems. Note, that the EKF does not produce an optimal estimator anymore. Although, it remains robust with respect to noise and is computationally cheap which makes it suitable for real-time applications.

A. System State Observation

A general external driving acceleration that has the form of white noise is assumed to affect the position of the target. The velocity $(\mathbf{V}(\tau))_{\tau\in\mathbb{R}^+}$ of the target is given in terms of a three-dimensional Brownian motion, also known as Wiener-process, $(\mathbf{W}_v(\tau))_{\tau\in\mathbb{R}^+}$ and its position $(\mathbf{Z}(\tau))_{\tau\in\mathbb{R}^+}$ is given by the integral over the Brownian motion. The increments of $\mathbf{W}_v$, e.g. $\mathbf{W}_v(t) - \mathbf{W}_v(s)$ with $0 \leq s < t$ are statistically independent and distributed as $\mathcal{N}(0,\, t-s)$. The stochastic differential equation linking the random acceleration and the velocity term can be solved as shown in [16].

$$\mathbf{V}(\tau) = \mathbf{V}_0 + \boldsymbol{\sigma}_v \mathbf{W}_v(\tau), \qquad \mathbf{Z}(\tau) = \mathbf{Z}_0 + \int_0^\tau \mathbf{V}(s)ds \tag{6}$$

Note, that $\mathbf{V}_0 = \mathbf{V}(0)$ and $\mathbf{Z}_0 = \mathbf{Z}(0)$ are constant vectors and denote the initial velocity and position of the object, respectively. The angular acceleration of the target is subject to independent white noise, so that the angular velocity $(\boldsymbol{\Omega}(\tau))_{\tau\in\mathbb{R}^+}$ is given by means of a three-dimensional Brownian motion $(\mathbf{W}_\omega(\tau))_{\tau\in\mathbb{R}^+}$.

$$\boldsymbol{\Omega}(\tau) = \boldsymbol{\Omega}_0 + \boldsymbol{\sigma}_\omega \mathbf{W}_\omega(\tau), \qquad \boldsymbol{\Theta}(\tau) = \boldsymbol{\Theta}_0 + \int_0^\tau \boldsymbol{\Omega}(s)ds \tag{7}$$

Here, $\boldsymbol{\Omega}_0 = \boldsymbol{\Omega}(0)$ and $\boldsymbol{\Theta}_0 = \boldsymbol{\Theta}(0)$ are constant vectors and denote the initial angular velocity and orientation of the target, respectively. The target can be observed at discrete times $t\Delta\tau,\ t \in \mathbb{N}$,

with time step $\Delta\tau$. Further, we denote the system states at time step $t\Delta\tau$ as $\mathbf{v}_t$, $\mathbf{z}_t$, $\boldsymbol{\omega}_t$ and $\boldsymbol{\theta}_t$. They can be represented using the recursive relations

$$\begin{aligned}
\mathbf{v}_t &= \mathbf{v}_{t-1} + \boldsymbol{\alpha}_t, & \boldsymbol{\alpha}_t &= \boldsymbol{\sigma}_v(\mathbf{W}_v(t\Delta\tau) - \mathbf{W}_v((t-1)\Delta\tau)) \\
\mathbf{z}_t &= \mathbf{z}_{t-1} + \mathbf{v}_{t-1}\Delta\tau + \boldsymbol{\beta}_t, & \boldsymbol{\beta}_t &= \boldsymbol{\sigma}_v \int_{(t-1)\Delta\tau}^{t\Delta\tau} (\mathbf{W}_v(\mathbf{s}) - \mathbf{W}_v((t-1)\Delta\tau))ds \\
\boldsymbol{\omega}_t &= \boldsymbol{\omega}_{t-1} + \boldsymbol{\gamma}_t, & \boldsymbol{\gamma}_t &= \boldsymbol{\sigma}_\omega(\mathbf{W}_\omega(t\Delta\tau) - \mathbf{W}_\omega((t-1)\Delta\tau)) \\
\boldsymbol{\theta}_t &= \boldsymbol{\theta}_{t-1} + \mathbf{v}_{t-1}\Delta\tau + \boldsymbol{\delta}_t, & \boldsymbol{\delta}_t &= \boldsymbol{\sigma}_\omega \int_{(t-1)\Delta\tau}^{t\Delta\tau} (\mathbf{W}_\omega(\mathbf{s}) - \mathbf{W}_\omega((t-1)\Delta\tau))ds
\end{aligned} \tag{8}$$

The increments of the Brownian motions are independent of each other and are summarized in

$$\mathbf{U}_t = \begin{bmatrix} \boldsymbol{\alpha}_t \\ \boldsymbol{\beta}_t \\ \boldsymbol{\gamma}_t \\ \boldsymbol{\delta}_t \end{bmatrix}. \tag{9}$$

The instances of $\mathbf{U}_t$ are independent and identically distributed with the multivariate normal distribution with zero mean and covariance matrix $\boldsymbol{\Sigma}$ given by

$$\boldsymbol{\Sigma} = \Delta\tau \begin{bmatrix} \boldsymbol{\sigma}_v^2\mathbf{I} & \frac{\boldsymbol{\sigma}_v^2}{2}\Delta\tau\mathbf{I} & \mathbf{0} & \mathbf{0} \\ \frac{\boldsymbol{\sigma}_v^2}{2}\Delta\tau\mathbf{I} & \frac{\boldsymbol{\sigma}_v^2}{3}\Delta\tau^2\mathbf{I} & \mathbf{0} & \mathbf{0} \\ \mathbf{0} & \mathbf{0} & \boldsymbol{\sigma}_\omega^2\mathbf{I} & \frac{\boldsymbol{\sigma}_\omega^2}{2}\Delta\tau\mathbf{I} \\ \mathbf{0} & \mathbf{0} & \frac{\boldsymbol{\sigma}_\omega^2}{2}\Delta\tau\mathbf{I} & \frac{\boldsymbol{\sigma}_\omega^2}{3}\Delta\tau^2\mathbf{I} \end{bmatrix}, \tag{10}$$

where $\mathbf{I}$ represents the three-dimensional identity matrix. The covariance matrix can be computed using Ito's lemma to account for the stochastic integrals [17]. The state vector

$$\mathbf{X}_t = \begin{bmatrix} \mathbf{v}_t \\ \mathbf{z}_t \\ \boldsymbol{\omega}_t \\ \boldsymbol{\theta}_t \end{bmatrix} \tag{11}$$

is linearly propagating satisfying

$$\mathbf{X}_t = \mathbf{F}\mathbf{X}_{t-1} + \mathbf{U}_t, \qquad \mathbf{F} = \begin{bmatrix} \mathbf{I} & \mathbf{0} & \mathbf{0} & \mathbf{0} \\ \Delta\tau\mathbf{I} & \mathbf{I} & \mathbf{0} & \mathbf{0} \\ \mathbf{0} & \mathbf{0} & \mathbf{I} & \mathbf{0} \\ \mathbf{0} & \mathbf{0} & \Delta\tau\mathbf{I} & \mathbf{I} \end{bmatrix}. \tag{12}$$

The magnetic field observation made at time t using (1) is denoted as $\mathbf{V}_t$. The magnetic field observation is also subject to additive noise $\mathbf{W}_t$. Note, that the system state $\mathbf{z}_t$ corresponds to the

position of the magnetic field source $\mathbf{x}_s$ and the system state $\boldsymbol{\theta}_t$ corresponds to the orientation of the magnetic dipole moment defined in (2) to (4). The velocity vectors $\mathbf{v}_t$ and $\boldsymbol{\omega}_t$ do not contribute to (1). To highlight the dependence upon $\mathbf{z}_t, \boldsymbol{\theta}_t$ the non-linear function $\mathbf{h}$ is introduced which corresponds to (1). Then together with (12) the system state and observation equations are given by

$$\mathbf{X}_t = \mathbf{F}\mathbf{X}_{t-1} + \mathbf{U}_t, \tag{13}$$

$$\mathbf{V}_t = \mathbf{h}(\mathbf{z}_t, \boldsymbol{\theta}_t) + \mathbf{W}_t. \tag{14}$$

B. Extended Kalman Filter

This section summarizes the well-known EKF approach [18], [19]. Consider a non-linear dynamical system with state propagation function f'_t depending on the system states X'_{t-1} and process noise $W'_t \sim \mathcal{N}(0, Q_t\prime)$ and the observation equation h'_t depending on X'_t and measurement noise $V'_t \sim \mathcal{N}(0, R'_t)$.

$$X'_t = f'_t(X'_{t-1}, W'_t) \tag{15}$$

$$Y'_t = h'_t(X'_t, V'_t) \tag{16}$$

The functions f'_t, h'_t are non-linear and differentiable. In general nothing can be said about the conditional distribution $X'_t|Y'_{1:t}$ due to the non-linearity. The EKF calculates an approximation of the conditional expectation by an appropriate linearization of the state transition and observation model. Due to the approximation, the resulting algorithm is not optimal in the least-squares sense. Let F'_X and F'_W be the partial derivatives of f' with respect to system state and process noise respectively. Further let H'_X and H'_V be the partial derivatives of h' with respect to system state and measurement noise respectively. The EKF algorithm is summarized below.

- Initialization:

$$\hat{x}'_{0|0} = E[X'_0],\ P'_{0|0} = cov(X'_0) \tag{17}$$

- Prediction:

$$\hat{x}'_{t|t-1} = f'(\hat{x}'_{t-1|t-1}, 0), \tag{18}$$

$$Y'_{e,t} = Y'_t - h'(\hat{x}'_{t|t-1}, 0), \tag{19}$$

$$P'_{t|t-1} = F'_X P'_{t-1|t-1} F'^T_X + F'_W Q'_t F'^T_W \tag{20}$$

- Update:

$$S'_t = H'_X P'_{t|t-1} H'^T_X + H'_V R'_t H'^t_V, \tag{21}$$

$$K'_t = P'_{t|t-1} H'^T_X S'^{-1}_t, \tag{22}$$

$$\hat{x}'_{t|t} = \hat{x}'_{t|t-1} + K'_t Y'_{e,t}, \tag{23}$$

$$P'_{t|t} = (I - K'_t H'_X) P'_{t-1|t-1} \tag{24}$$

C. Tracking Experiments

In this section the performance of the EKF based tracking is investigated. As mentioned a number of unique measurements is required due to the model complexity. Therefore, three emitters and one sensor is used. The sensor is measuring the three-dimensional field at a known spatial point. The emitters are static to each other. However, in a global coordinate frame the vector between the emitters is not static due to the rotation of the object. Without the presence of rotation the distance between first emitter s_1 and second emitter s_2 is given by $\mathbf{p}_{12} = [0.05,\ 0.05,\ 0.05]^T$. The distance between first and third emitter s_3 is given by $\mathbf{p}_{13} = [-0.02,\ 0.03,\ 0.02]^T$. The position of s_1 is used as target position $\mathbf{x}_s$ following the trajectory simulated according to (8). A period of $20\,\mathrm{s}$ using $\Delta\tau = 0.1\,\mathrm{s}$ with parameters $\boldsymbol{\sigma}_v = 0.01, \boldsymbol{\sigma}_\theta = 0.1$ and initial state $\mathbf{X}_0 = [\mathbf{v}_0,\ \mathbf{z}_0,\ \boldsymbol{\omega}_0,\ \boldsymbol{\theta}_0]$ is simulated.

$$\mathbf{v}_0 = [0.01,\ 0,\ -0.005]^T, \quad \mathbf{z}_0 = [0.2,\ -0.2,\ 0.3]^T, \quad \boldsymbol{\omega}_0 = [0,\ 0,\ 0]^T, \quad \boldsymbol{\theta}_0 = [0.02,\ -0.05,\ \frac{\pi}{4}]^T$$

The measurement data $\mathbf{V}_t$ is generated first calculating the magnetic field using (1) and then adding white noise. The receiver $\mathbf{x}_r$ is located in the origin. Note, that the emitters are used in a time-multiplexed fashion, thus only one emitter is transmitting at any instant in time. Additionally, the magnetic dipole moment of each emitter is $1\,\mathrm{Am}^2$ and they point towards orthogonal directions. The initial guess of $\mathbf{X}_0$ for the EKF is $\hat{\mathbf{X}}_0 = [\hat{\mathbf{v}}_0,\ \hat{\mathbf{z}}_0,\ \hat{\boldsymbol{\omega}}_0,\ \hat{\boldsymbol{\theta}}_0]$ given by

$$\hat{\mathbf{v}}_0 = [0,\ 0,\ 0]^T, \quad \hat{\mathbf{z}}_0 = [0.05,\ -0.1,\ 0.4]^T, \quad \hat{\boldsymbol{\omega}}_0 = [0,\ 0,\ 0]^T, \quad \hat{\boldsymbol{\theta}}_0 = [0,\ 0,\ 1]^T.$$

Note that (13) is linear, therefore, in order to apply the EKF only (14) needs to be linearised. This can be done by calculating the partial derivatives of $\mathbf{h}$ with respect to $\mathbf{X}_t$. The tracking performance of the EKF in terms of position $\hat{\mathbf{x}}_s$ is shown in Fig. 2 and in terms of orientation $\hat{\boldsymbol{\theta}}$ is reported in Fig. 3. It can be seen, that true system state can be found, despite the poor initial guess. The tracking accuracy decays with increasing distance to the receiver. This is explained

by the decreasing signal to noise ratio of the measured magnetic field. The orientation is resolved to $-\pi \leq \boldsymbol{\theta} < \pi$ which justifies the orientation jumps.

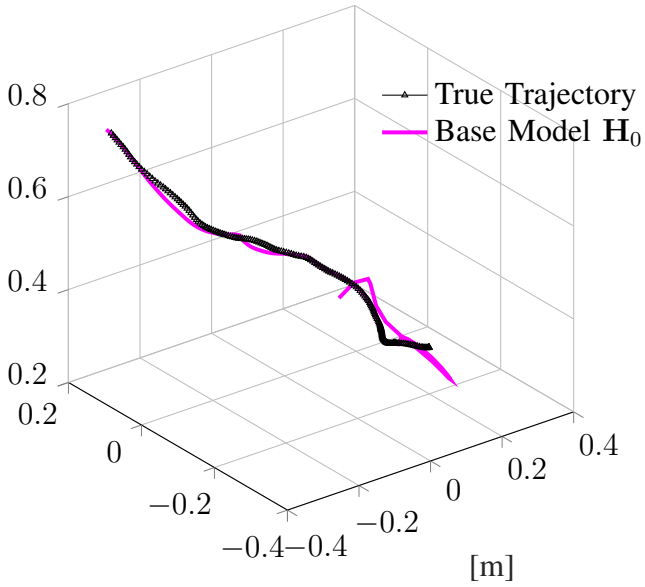

Fig. 2. A magnetic field source is moving along a random trajectory, indicated with black markers, driven by Brownian motion. The EKF estimates the trajectory shown as magenta waveform. The algorithm is able to identify the true states, despite its poor initial guess.

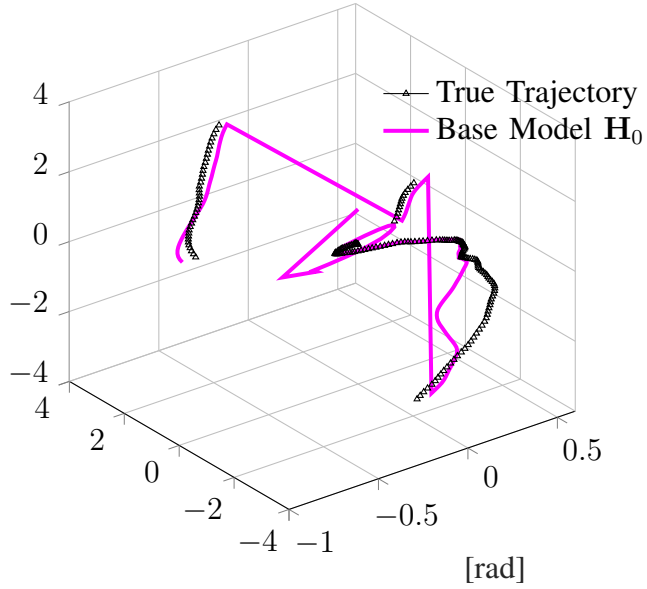

Fig. 3. While moving along the trajectory the orientation of the magnetic field source is changing by means of a three-dimensional Brownian motion. The true orientation is indicated with black markers whereas the estimated orientation is shown as magenta waveform. Note, that the x-value, y-value and z-value represent the rotation around x, y and z-axis respectively.

IV. Eddy Current Model

The previous chapter showed, that a stack of moving magnetic field source can be tracked using an EKF. However, conductive objects in the vicinity of the sensor are not considered and may distort the pose estimation, because the magnetic field is altered and is not accurately modelled by (1) anymore. Often the carrier of the emitter, e.g. UAV or wheeled robot is made of conductive materials. This chapter introduces a methodology to suppress the influence of those known conductive objects. Suppose that there is an electromagnetic inclusion in $\mathbb{R}^3$ of the form B, where B is a bounded, smooth domain. Let the constant quantities $\mu_\star$ and $\sigma_\star$ denote the

permeability and the conductivity of the inclusion. The piecewise constant magnetic permeability and electric conductivity is given by

$$\mu_a = \begin{cases} \mu_\star & \text{in } B \\ \mu_0 & \text{in } B^c = \mathbb{R}^3 \setminus B \end{cases} \qquad \sigma_a = \begin{cases} \sigma_\star & \text{in } B \\ \sigma_0 & \text{in } B^c. \end{cases} \tag{25}$$

Let $(\mathbf{E}_a, \mathbf{H}_a)$ denote the eddy current fields in presence of the electromagnetic inclusion B and a source current $\mathbf{J}_0$ located outside the inclusion. It is supposed that $\mathbf{J}_0$ is divergence free $\nabla \cdot \mathbf{J}_0 = 0$ in $\mathbb{R}^3$. The fields $(\mathbf{E}_a, \mathbf{H}_a)$ are the solutions of the following eddy current equations

$$\begin{cases} \nabla \times \mathbf{E}_a = i\omega\mu_a \mathbf{H}_a & \text{in } \mathbb{R}^3 \\ \nabla \times \mathbf{H}_a = \sigma_a \mathbf{E}_a + \mathbf{J}_0 & \text{in } \mathbb{R}^3 \\ \mathbf{E}_a(\mathbf{x}) = \mathcal{O}(|\mathbf{x}|^{-1}), \quad \mathbf{H}_a(\mathbf{x}) = \mathcal{O}(|\mathbf{x}|^{-1}) & \text{as } |\mathbf{x}| \to \infty. \end{cases} \tag{26}$$

Commonly, FEMs based simulation environments are used to solve (26) for $\mathbf{H}_a$. Those approaches come with high computational cost and are often not applicable in low-power real-time devices. In the applied mathematics community the change in magnetic field $\tilde{\mathbf{H}}_a = \mathbf{H}_a - \mathbf{H}_0$ due to the presence of the object B is explicitly expressed given by (27). The proof can be found in [10].

$$\tilde{\mathbf{H}}_a(\mathbf{x}_r) = \int_B \nabla_{\mathbf{x}_r} G(\mathbf{x}_r, \mathbf{y}) \times \nabla_{\mathbf{y}} \times \tilde{\mathbf{H}}_a(\mathbf{y}) d\mathbf{y} + (1 - \frac{\mu_\star}{\mu_0}) \int_B (\mathbf{H}_a(\mathbf{y}) \cdot \nabla_{\mathbf{y}}) \nabla_{\mathbf{x}_r} G(\mathbf{x}_r, \mathbf{y}) d\mathbf{y} \tag{27}$$

Here, $\mathbf{x}_r$ denotes the point of observation, where $\mathbf{x}_r \in B^c$. The scalar function $G(\mathbf{x}_r, \mathbf{y})$ represents the fundamental solution of the Laplace equation given by

$$G(\mathbf{x}_r, \mathbf{y}) = \frac{1}{4\pi |\mathbf{x}_r - \mathbf{y}|}. \tag{28}$$

In the following sections it is shown that this formula is especially useful for objects which are static with respect to the emitter. In such a situation the curl of $\tilde{\mathbf{H}}_a(\mathbf{y})$ as well as the field $\mathbf{H}_a(\mathbf{y})$ are constant.

A. Numerical Experiments and Verification

This section investigates the accuracy of the formula given in (27) by comparing it with the classical FEM based approach. Therefore, a cube made of copper is centred at $[0\ 0\ 0.15]^T$. Its electrical conductivity and edge length is given by $\sigma_\star = 59.9 \times 10^6\ \frac{\mathrm{S}}{\mathrm{m}}$ and $0.05\,\mathrm{m}$, respectively. The used magnetic permeability is $\mu_\star = \mu_0 = 4\pi \times 10^{-7}\ \frac{\mathrm{H}}{\mathrm{m}}$. The first emitter is located at

$[0\ 0\ 0.2]^T$. The distances to second and third emitter are reused from the previous section, given by $\mathbf{p}_{12}$ and $\mathbf{p}_{13}$. The corresponding dipole moments are

$$\mathbf{m}_0 = \begin{bmatrix} 0 \\ 0 \\ 0.01 \end{bmatrix} \quad \mathbf{m}_1 = \begin{bmatrix} 0 \\ 0.01 \\ 0 \end{bmatrix} \quad \mathbf{m}_2 = \begin{bmatrix} 0.01 \\ 0 \\ 0 \end{bmatrix} \quad \mathrm{Am}^2.$$

The point of observation $\mathbf{x}_r$ is located at $[0.05\ 0.05\ 0.2]^T$. As a reference, a commercial FEM based software-kit is used [20]. The simulation runs once in presence and once in absence of the copper cube and calculates the magnetic field at $\mathbf{x}_r$. The magnetic field difference represents the reference result $\tilde{\mathbf{H}}_r$. It is worth noting, that boundary conditions regarding the simulation environment border are avoided by extending the mesh until the field drops below the numerical boundary.

The explicit formula (27) is used to obtain a comparative result. Therefore, the curl of the magnetic field in the conductive object is pre-computed using the presented FEM environment. Since the object is statically linked to the field emitter, the field curl at the object is independent of the global position and orientation. The curl of the magnetic field in absence of the magnetic field can be calculated analytically.

TABLE I

A COMPARISON OF THE FEM BASED SOLUTION WITH THE EXPLICIT FORMULA. THE USED OBJECT PARAMETERS ARE $\sigma_\star = 59.9 \times 10^6\ \frac{\mathrm{S}}{\mathrm{m}}$ AND $\mu_\star = \mu_0 = 4\pi \times 10^{-7}\ \frac{\mathrm{H}}{\mathrm{m}}$.

		x-component	**y-component**	**z-component**
Emitter 1	FEM solution $\tilde{\mathbf{H}}_r$	$230.310\,\mathrm{mT}$	$217.780\,\mathrm{mT}$	$-123.660\,\mathrm{mT}$
	Explicit solution $\tilde{\mathbf{H}}_a$	$227.340\,\mathrm{mT}$	$223.630\,\mathrm{mT}$	$-119.120\,\mathrm{mT}$
Emitter 2	FEM solution $\tilde{\mathbf{H}}_r$	$17.742\,\mathrm{mT}$	$4.450\,\mathrm{mT}$	$-4.174\,\mathrm{mT}$
	Explicit solution $\tilde{\mathbf{H}}_a$	$17.821\,\mathrm{mT}$	$4.260\,\mathrm{mT}$	$-3.628\,\mathrm{mT}$
Emitter 3	FEM solution $\tilde{\mathbf{H}}_r$	$-19.831\,\mathrm{mT}$	$-10.634\,\mathrm{mT}$	$-25.090\,\mathrm{mT}$
	Explicit solution $\tilde{\mathbf{H}}_a$	$-19.287\,\mathrm{mT}$	$-9.726\,\mathrm{mT}$	$-26.752\,\mathrm{mT}$

As shown in Tab. I the classical FEM based approach and (27) obtain similar results. The minor discrepancies are mostly explained by numerical inaccuracies. It is worth noting, that the magnetic field components at the observation point changed by approximately 50% due to the presence of the copper cube. The imaginary part of the field is negligible small for diamagnetic materials. To show the validity of the explicit formula, a second scenario is presented with

$\sigma_\star = 0.1 \times 10^6 \, \frac{\mathrm{S}}{\mathrm{m}}$ and $\mu_\star = 100 \cdot \mu_0$. The geometric configuration is reused and the corresponding results are reported in Tab. II. It is shown, that (27) generates the same result then the classical FEM based approach for both imaginary and real part of the magnetic field.

TABLE II

A COMPARISON OF THE FEM BASED SOLUTION WITH THE EXPLICIT FORMULA. THE USED OBJECT PARAMETERS ARE $\sigma_\star = 0.1 \times 10^6 \, \frac{\mathrm{S}}{\mathrm{m}}$ AND $\mu_\star = 100 \cdot \mu_0 = 4\pi \times 10^{-5} \, \frac{\mathrm{H}}{\mathrm{m}}$.

		x-component	**y-component**	**z-component**
Emitter 1	FEM solution $\tilde{\mathbf{H}}_r$	$(-248.620 + 91.751\mathrm{i})\,\mathrm{mT}$	$(-245.780 + 88.301\mathrm{i})\,\mathrm{mT}$	$(379.540 - 71.226\mathrm{i})\,\mathrm{mT}$
	Explicit solution $\tilde{\mathbf{H}}_a$	$(-247.620 + 90.374\mathrm{i})\,\mathrm{mT}$	$(-247.240 + 88.652\mathrm{i})\,\mathrm{mT}$	$(373.891 - 69.934\mathrm{i})\,\mathrm{mT}$
Emitter 2	FEM solution $\tilde{\mathbf{H}}_r$	$(13.957 + 8.412\mathrm{i})\,\mathrm{mT}$	$(-228.560 + 2.317\mathrm{i})\,\mathrm{mT}$	$(-1.376 - 2.981\mathrm{i})\,\mathrm{mT}$
	Explicit solution $\tilde{\mathbf{H}}_a$	$(13.712 + 8.236\mathrm{i})\,\mathrm{mT}$	$(-232.007 + 2.268\mathrm{i})\,\mathrm{mT}$	$(-1.643 - 2.874\mathrm{i})\,\mathrm{mT}$
Emitter 3	FEM solution $\tilde{\mathbf{H}}_r$	$(-86.642 - 10.840\mathrm{i})\,\mathrm{mT}$	$(57.967 - 6.754\mathrm{i})\,\mathrm{mT}$	$(-398.010 - 11.367\mathrm{i})\,\mathrm{mT}$
	Explicit solution $\tilde{\mathbf{H}}_a$	$(-86.256 - 10.581\mathrm{i})\,\mathrm{mT}$	$(59.167 - 6.668\mathrm{i})\,\mathrm{mT}$	$(-395.791 - 11.422\mathrm{i})\,\mathrm{mT}$

B. Adapted EKF Model

This section describes how the EKF based tracking approach is adapted with respect to the presented eddy current scenario. The formula given in (27) consists mainly of 2 parts, where the second part corrects for the effects of ferro-magnetic objects. As a starting point the first part is analysed and given by $\int_B \nabla_{\mathbf{x}_r} G(\mathbf{x}_r, \mathbf{y}) \times \nabla_{\mathbf{y}} \times \tilde{\mathbf{H}}_a(\mathbf{y}) d\mathbf{y}$. By introducing a second coordinate frame the integral can be simplified. The first coordinate frame is from now on called global frame and the second coordinate frame is called local frame. The local frame has its origin at the position of the first emitter. The local coordinate frame can freely move and change its orientation with respect to the global frame frame which is assumed to be fixed. Consequently, the target of the tracking algorithm is the origin of the local frame expressed in the global frame. For simplicity, the volume integral over the conductive object is defined in the local coordinate frame where its limits are constant due to the static link between the target and the object.

Further, the object B is separated into a number n of smaller objects B_i with $i = 1...n$, where $B_i \subset B$ and $B_i \cap B_j = \emptyset$ with $j = 1...n$ and $i \neq j$. The volume integral can then be rewritten as

$$\int_B \nabla_{\mathbf{x}_r} G(\mathbf{x}_r, \mathbf{y}) \times \nabla_{\mathbf{y}} \times \tilde{\mathbf{H}}_a(\mathbf{y}) d\mathbf{y} = \sum_{i=1}^{n} \left(\int_{B_i} \nabla_{\mathbf{x}_r} G(\mathbf{x}_r, \mathbf{y_i}) \times \nabla_{\mathbf{y}_i} \times \tilde{\mathbf{H}}_a(\mathbf{y}_i) d\mathbf{y}_i \right). \tag{29}$$

The EKF based tracking approach becomes applicable when $\mathbf{y_i}$ is fixed to the geometric center of B_i called $\overline{\mathbf{y}}_i$. This introduces an quantization error when calulating (27). However, as n tends

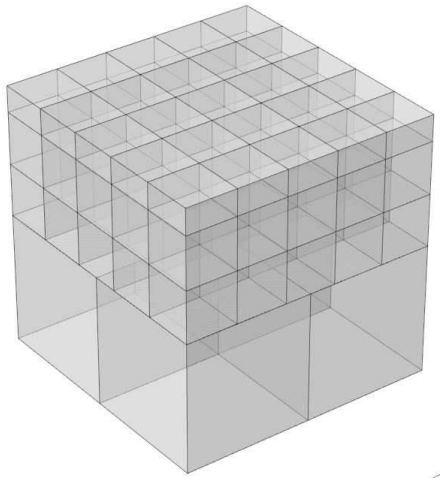

Fig. 4. The conductive object in the vicinity of the sensor is divided into smaller objects. The top surface, showing increased object resolution, points towards the magnetic field sources.

to grow towards infinity and B_i shrinks towards zero the error would vanish. As a consequence of the quantization, $\nabla_{\mathbf{x}_r} G(\mathbf{x}_r, \overline{\mathbf{y}}_i)$ becomes independent of the integration which results in

$$\sum_{i=1}^{n} (\int_{B_i} \nabla_{\mathbf{x}_r} G(\mathbf{x}_r, \mathbf{y_i}) \nabla_{\mathbf{y}_i} \times \tilde{\mathbf{H}}_a(\mathbf{y}_i) d\mathbf{y}_i) \approx \sum_{i=1}^{n} (\nabla_{\mathbf{x}_r} G(\mathbf{x}_r, \overline{\mathbf{y}}_i) \times \int_{B_i} \nabla_{\mathbf{y}_i} \times \tilde{\mathbf{H}}_a(\mathbf{y}_i) d\mathbf{y}_i). \quad (30)$$

The integral over $\nabla_{\mathbf{y}_i} \times \tilde{\mathbf{H}}_a(\mathbf{y}_i)$ is constant and can be pre-computed, which results in $\tilde{\mathbf{H}}_{C_i}$. A proper discretization for this approximation has to be found for any individual object geometry and constellation with respect to the emitters. The used discretization for the copper cube is schematically shown in Fig. 4. The parts of the cube which are closer to the emitter are more significant. Therefore, the surface with higher object resolution points towards the emitter. A higher object resolution would increase accuracy of (30) and is therefore favourable. However, this comes with additional computational cost.

The described procedure is also applied to the second part of the formula. Contrary, the integral over the magnetic field instead of the curl of the magnetic field is required to be pre-computed. In total, for large n and small B_i a good approximation of (27) is given by

$$\tilde{\mathbf{H}}_a(\mathbf{x}_r) \approx \sum_{i=1}^{n} (\nabla_{\mathbf{x}_r} G(\mathbf{x}_r, \overline{\mathbf{y}}_i) \times \tilde{\mathbf{H}}_{C_i}) + (1 - \frac{\mu_\star}{\mu_0}) \sum_{i=1}^{n} (\mathbf{H}_i \cdot \nabla_{\overline{\mathbf{y}}_i)} \nabla_{\mathbf{x}_r} G(\mathbf{x}_r, \overline{\mathbf{y}}_i). \quad (31)$$

Here, $\mathbf{H}_i$ denotes the volume integral over the magnetic field in B_i in presence of the object. In the global frame the quantity $\overline{\mathbf{y}}_i$ can be expressed as $\overline{\mathbf{y}}_i = \mathbf{r} + \mathbf{R}\mathbf{z}_i$ with $\mathbf{z}_i$ being the known distance (in local frame) between the emitter and the geometric center of B_i. Note, that the

known point of observation $\mathbf{x}_r$ is defined in the global coordinate system, which result in 6 remaining DOF, i.e. $\mathbf{x}_s$ and $\boldsymbol{\theta}$.

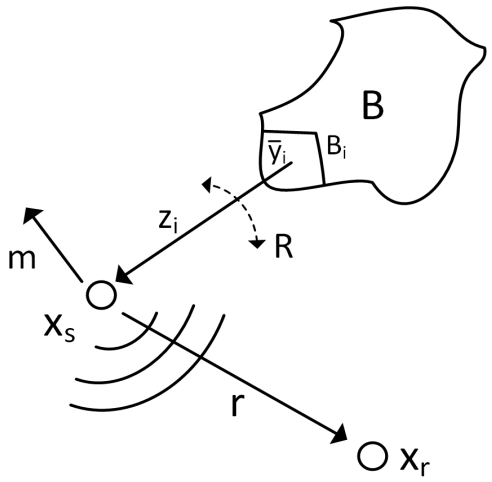

Fig. 5. The geometric dependencies are schematically shown. Here, $\mathbf{x}_r$ represents the point of observation defined in global coordinate system, $\mathbf{x}_s$ represents the magnetic field source and origin of the local coordinate frame. Further, $\mathbf{z}_i$ given in local frame denotes the vector between geometric center of object part B_i and magnetic field source. The limits of object B are known in local frame. The transition between local and global coordinate frame is defined by translation $\mathbf{r}$ and rotation $\mathbf{R}$.

The geometric dependencies are schematically visualized in Fig. 5. Although, Fig. 5 shows a 2-D setup the same relations hold for the 3-D case. The magnetic field at $\mathbf{x}_r$ is ultimately given by

$$\mathbf{H}(\mathbf{x}_r) = \mathbf{H}_0(\mathbf{r}, \mathbf{m}) + \tilde{\mathbf{H}}_a(\mathbf{x}_r). \tag{32}$$

The non-linear function $\mathbf{h}$ from (14) clearly corresponds now to (32). To apply the EKF, it needs to be linearised with respect to the system states $\mathbf{X}_t$.

C. Tracking Experiments

This section compares the EKF based tracking performance of the model extended for close conductive objectes (32) with the model given by (1). Note, that a conductive cube, shown in Fig. 4 is located close to the magnetic field sources. Most of the used parameters of this experiments are reused from Section III-C. However, the starting point of the trajectory $\mathbf{X}_0$ is in this experiment given by

$$\mathbf{v}_0 = [0.001,\ 0.001,\ 0.001]^T, \quad \mathbf{z}_0 = [0,\ 0,\ 0.2]^T, \quad \boldsymbol{\omega}_0 = [0,\ 0,\ 0]^T, \quad \boldsymbol{\theta}_0 = [0,\ 0,\ 0]^T.$$

To get a meaningful comparison the initial guess of the EKF is equal to the initial position $\hat{\mathbf{X}}_0 = \mathbf{X}_0$. The edge length of the conductive cube B is $5\,\mathrm{cm}$ and its center is located at $[0,\ 0,\ 0.15]^T$. The geometry is separated into $n = 79$ smaller cubes B_i, shown in Fig. 4. The integrals over the curl of the magnetic field resulting in $\tilde{\mathbf{H}}_{C_i}$ and the integrals over the magnetic field resulting in $\mathbf{H}_i$ are pre-computed. For zero conductivity and permeability the model $\mathbf{H}_0$ and $\mathbf{H}$ have the same result. First, a comparison is made were the conductivity of the cube is changed to $\sigma_\star = 1000\,\frac{\mathrm{S}}{\mathrm{m}}$, which is approximately the conductivity of various carbon based materials.

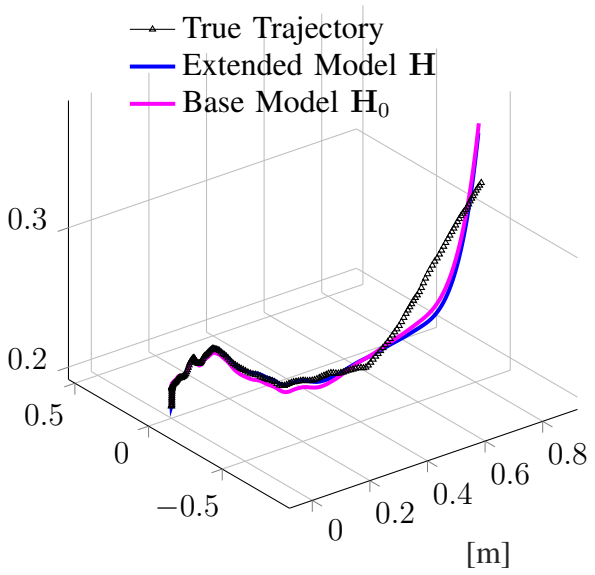

Fig. 6. The EKF based position tracking is shown with two different underlying models. The black markers indicate the true position, the magenta waveform represents the underlying model (1), whereas the blue waveform shows the tracking based on the extended model (32). Due to the low conductivity of the object ($\sigma_\star = 1000\,\frac{\mathrm{S}}{\mathrm{m}}$), the accuracy of both models is almost equal.

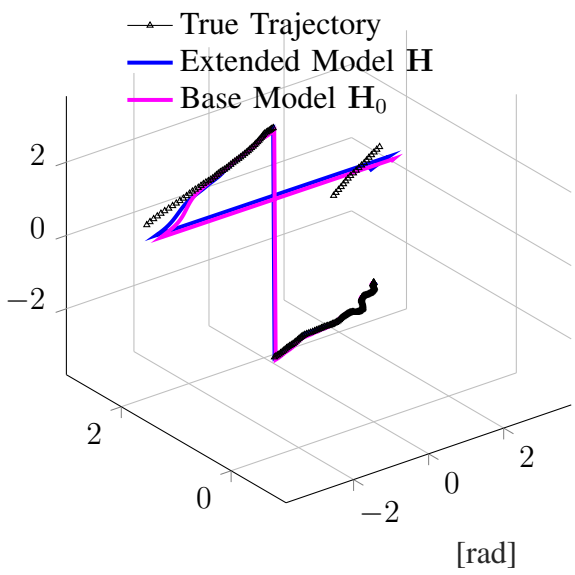

Fig. 7. The EKF based orientation tracking is shown with two different underlying models. The waveform colors and underlying models are defined as in Fig. 6. Due to the low conductivity of the object ($\sigma_\star = 1000\,\frac{\mathrm{S}}{\mathrm{m}}$), the accuracy of both models is almost equal.

The estimated trajectory and orientation using both models as well as the true trajectory and true orientation is reported in Fig. 6 and Fig. 7, respectively. It is observable, that for the used conductivity the performance of both models is acceptable. The trajectory and the orientation of the target is well tracked. However, the mean squared error of the adapted model is slightly lower.

To visualize the advantages of the $\mathbf{H}$ model the conductivity of B is increased to the level of copper $\sigma_\star = 59.9 \times 10^6 \, \frac{\mathrm{S}}{\mathrm{m}}$. The evolution of the position and orientation estimates using both models are reported in Fig. 8 and Fig. 9, respectively. The EKF tracking accuracy based on the $\mathbf{H}_0$ model decreased dramatically, while for the adapted model $\mathbf{H}$ the tracking remains accurate. Here, the benefit in terms of accuracy of the comparatively complex model extension is clearly visible. The extended model is able to accurately track the trajectories until the receiver signal strength becomes too weak and measurement noise starts to dominate. The base model which neglects the highly conductive cube performs insufficient even in the areas where the receiver signal strength is still reasonable.

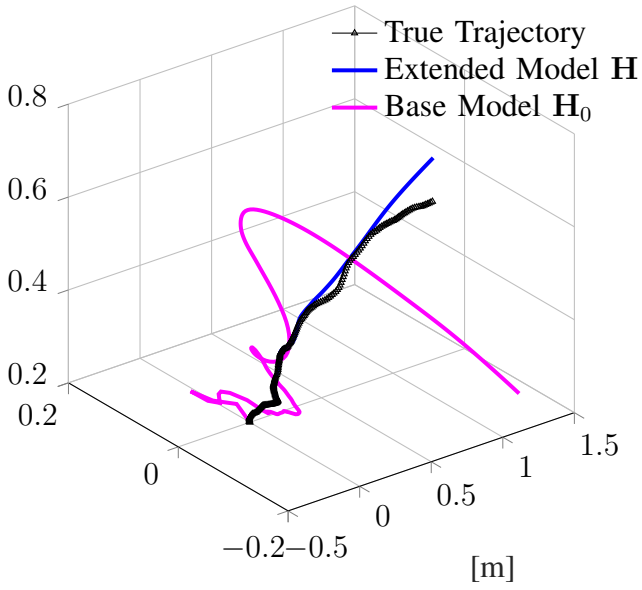

Fig. 8. The EKF based position tracking is shown with two different underlying models. The black markers indicate the true position, the magenta waveform represents the underlying model (1) which holds for surrounding air, whereas the blue waveform shows the superior tracking performance based on the extended model (32) for close-by conductive objects. The conductivity of the cube is $\sigma_\star = 59.9 \times 10^6 \, \frac{\mathrm{S}}{\mathrm{m}}$.

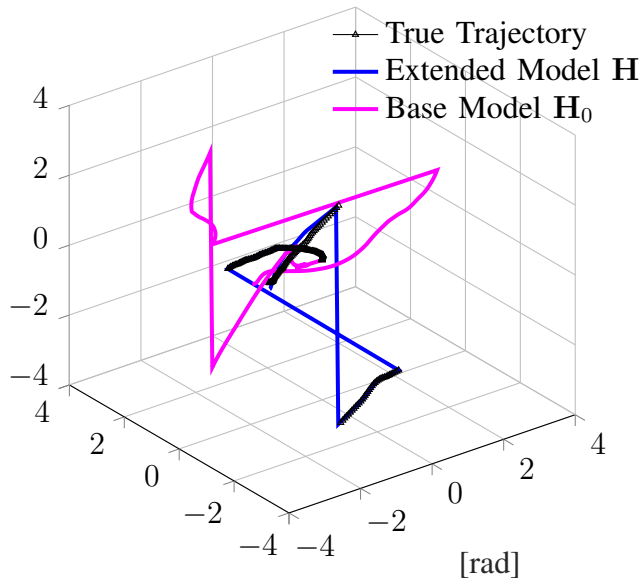

Fig. 9. The EKF based orientation tracking is shown with two different underlying models. The waveform colors and underlying models are defined as in Fig. 8. Due to the high conductivity of the object ($\sigma_\star = 59.9 \times 10^6 \, \frac{\mathrm{S}}{\mathrm{m}}\mathrm{m}$), the extended model performs superior.

A third experiment with parameters $\sigma_\star = 0.1 \times 10^6 \, \frac{\mathrm{S}}{\mathrm{m}}$ and $\mu_\star = 100 \cdot \mu_0$ is carried out. In Fig. 10 and Fig. 11 it is shown that the tracking performance is maintained for ferro-magnetic objects. A comparison with the traditional model (1) is neglected because it diverges immediately. Additionally, note that the introduced phase shift, also shown in Tab. II, may be difficult to measure with common sensors. However, it can easily be estimated when emitter and receiver are synchronized.

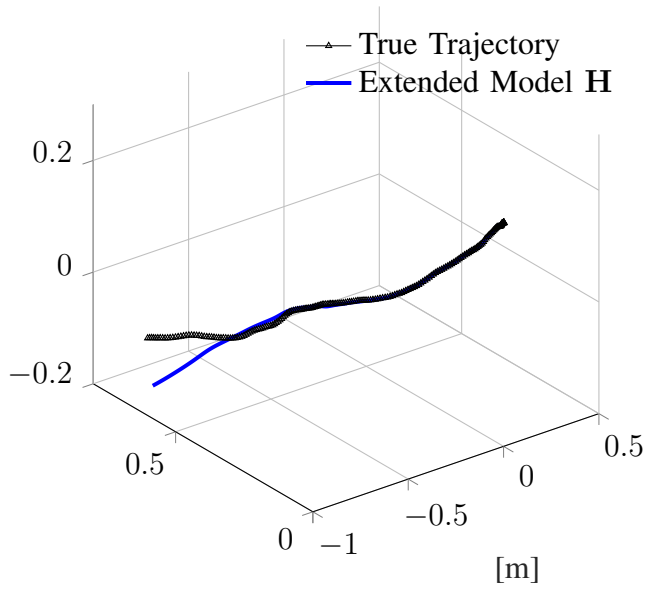

Fig. 10. The black markers indicate the true position and the blue waveform represents the EKF based position tracking for the extended model (32) which holds for close-by conductive and ferro-magnetic materials. The conductivity and permeability of the cube is $\sigma_\star = 0.1 \times 10^6 \, \frac{\mathrm{S}}{\mathrm{m}}$ and $\mu_\star = 100 \cdot \mu_0$, respectively.

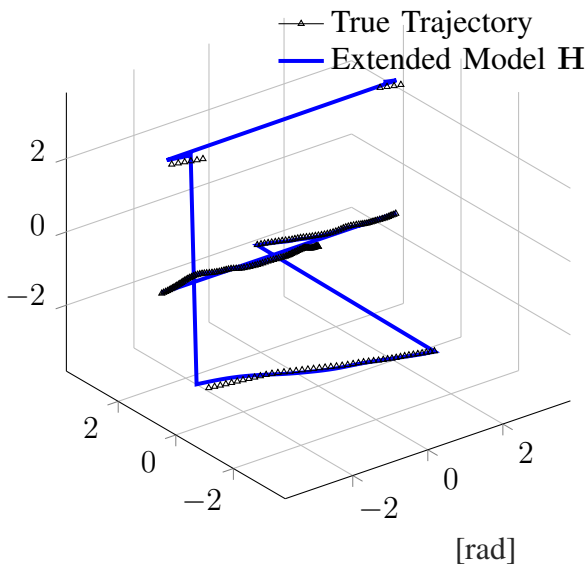

Fig. 11. The black markers indicate the true orientation and the blue waveform represents the EKF based orientation tracking for the extended model (32) which holds for close-by conductive and ferro-magnetic materials. The conductivity and permeability of the cube is $\sigma_\star = 0.1 \times 10^6 \, \frac{\mathrm{S}}{\mathrm{m}}$ and $\mu_\star = 100 \cdot \mu_0$, respectively.

In the last experiment a trajectory, which is not randomly generated is used. Instead of using the Brownian motion model from (8) a helical line with constant vertical velocity is used. Additionally, the angular velocity is constant, but its x and y components vary periodically. Note, that the attitude of the target is always aligned to the flight direction. The system model remains the same and is designed for random trajectories. The flight path simulates non-random real-world movement, e.g. a UAV in the vicinity of the sensor. The initial states $\mathbf{X}_0$ are given by

$$\mathbf{v}_0 = [0,\ 0.12,\ 0.02]^T, \quad \mathbf{z}_0 = [0.6,\ 0,\ 0]^T, \quad \boldsymbol{\omega}_0 = [0,\ 0,\ 0.02]^T, \quad \boldsymbol{\theta}_0 = [0.1662,\ 0,\ 0.02]^T.$$

The initial guess of the EKF is $\hat{\mathbf{X}}_0 = \mathbf{X}_0$. The conductive cube is made of copper with $59.9 \times 10^6 \, \frac{\mathrm{S}}{\mathrm{m}}$ and $\mu_\star = \mu_0$. It's location and size is reused from the previous experiments. The simulated flight lasts $80\,\mathrm{seconds}$ and its trajectory is given by

$$\boldsymbol{z}(t) = \begin{bmatrix} 0.6\cos(0.2t) \\ 0.6\sin(0.2t) \\ 0.01t \end{bmatrix}, \qquad \boldsymbol{\theta}(t) = \begin{bmatrix} 0.1662 \\ 0 \\ 0.02t \end{bmatrix}. \tag{33}$$

The evolution of the position and orientation estimates are shown in Fig. 12 and Fig. 13, respectively. The estimator accurately tracks the non-random helical trajectory until the received signal strength becomes too weak caused by the increasing distance to the transmitter. This shows, that the approach is valid for tracking moving targets such as wheeled robots or UAVs. Especially, landing scenarios under harsh conditions of UAVs can be greatly supported. The electromagnetic tracking approach is unaffected by many detrimental influences such as rain, fog or bad illumination.

V. Conclusion

In this paper, a 6-DOF pose estimation principle based on electromagnetic fields is presented. It is especially useful for autonomous systems operating under harsh conditions such as denied line of sight, bad light conditions, rain, fog or when navigating close to objects. The system consists of two parts, a transmitter and a receiver with known pose. The pose of the transmitter, which is e.g. mounted on a mobile platform is estimated. The systems accuracy increases with decreasing distance, which makes it especially beneficial for landing scenarios of UAVs. This work additionally introduces a methodology to account for conductive and ferro-magnetic objects

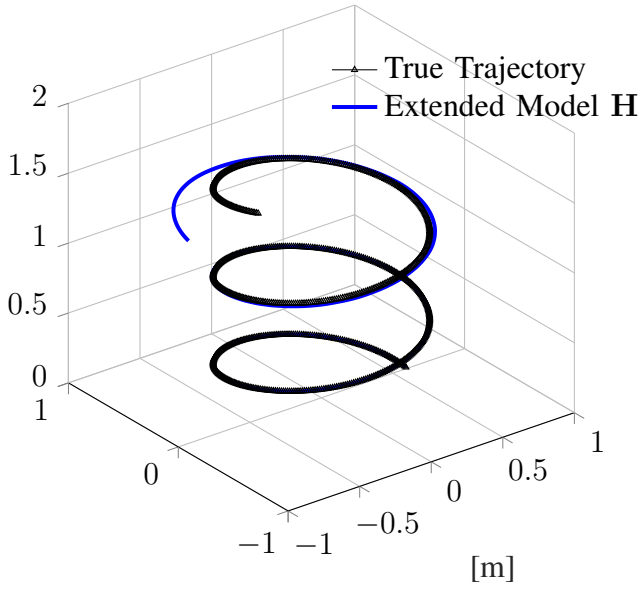

Fig. 12. The black markers indicate the true trajectory and the blue waveform represents the EKF estimates with underlying model (32). The conductivity of the close-by copper cube is $\sigma_\star = 59.9 \times 10^6 \, \frac{\mathrm{S}}{\mathrm{m}}$. The used trajectory is not randomly chosen, despite the model formulation which expects random motion.

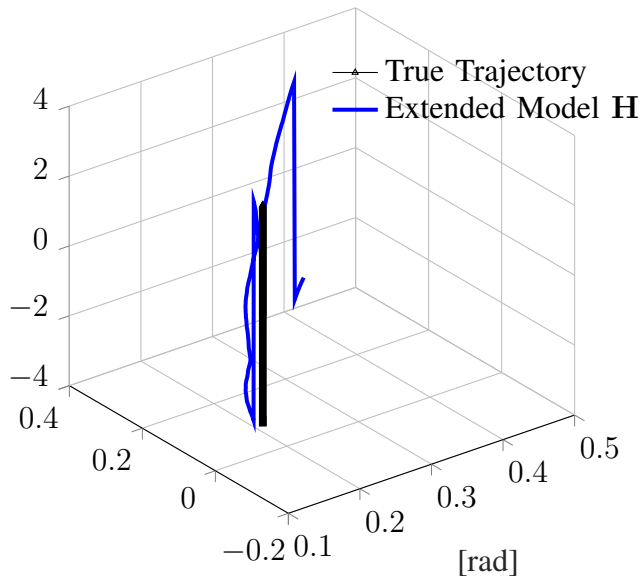

Fig. 13. The black markers indicate the true trajectory and the blue waveform represents the EKF estimates with underlying model (32). The conductivity of the close-by copper cube is $\sigma_\star = 59.9 \times 10^6 \, \frac{\mathrm{S}}{\mathrm{m}}$. The used trajectory is not randomly chosen, despite the model formulation which expects random motion.

in the vicinity of the sensor which alter the electromagnetic field due to eddy currents. An explicit formula is introduced, which allows for EKF based real-time tracking. The explicit expression is compared to a FEM based solution of the full Maxwell equations and accuracy is verified. Lastly, the superior tracking performance of the EKF based on the extended model is reported.

ACKNOWLEDGMENT

The research leading to these results has received funding from the Swiss National Science Foundation under the grant 200021–172483.

REFERENCES

[1] Bloesch M., Burri M., Omari S., Hutter M. and Siegwart R. (2017). Iterated extended Kalman filter based visual-inertial odometry using direct photometric feedback. The International Journal of Robotics Research, 36(10), 1053–1072.

[2] Hausman K., Weiss S. Brockers R., Matthies L. and Sukhatme G. (2016). Self-Calibrating Multi-Sensor Fusion with Probabilistic Measurement Validation for Seamless Sensor Switching on a UAV. 10.1109/ICRA.2016.7487626.

[3] Heydariaan M., Mohammadmoradi H. and Gnawali O. (2018). Toward Standard Non-Line-of-Sight Benchmarking of Ultra-Wideband Radio-Based Localization. 19-24. 10.1109/CPSBench.2018.00010.

[4] Zhang C., Kuhn M. J., Merkl B. C., Fathy A. E. and Mahfouz M. R., "Real-Time Noncoherent UWB Positioning Radar With Millimeter Range Accuracy: Theory and Experiment," in IEEE Transactions on Microwave Theory and Techniques, vol. 58, no. 1, pp. 9-20, Jan. 2010.

[5] Yun X., Bachmann E. R. and McGhee R. B., "A Simplified Quaternion-Based Algorithm for Orientation Estimation From Earth Gravity and Magnetic Field Measurements," in IEEE Transactions on Instrumentation and Measurement, vol. 57, no. 3, pp. 638-650, March 2008.

[6] Schlegl T., Neumayer M., Mühlbacher-Karrer S. and Zangl H., "A Pretouch Sensing System for a Robot Grasper Using Magnetic and Capacitive Sensors," in IEEE Transactions on Instrumentation and Measurement, vol. 62, no. 5, pp. 1299-1307, May 2013.

[7] Than T. D., Alici G., Zhou H. and Li W., "A Review of Localization Systems for Robotic Endoscopic Capsules," in IEEE Transactions on Biomedical Engineering, vol. 59, no. 9, pp. 2387-2399, Sept. 2012.

[8] Gietler H., Böhm C., Mitterer T., Faller L.-M., Weiss S. and Zangl H., *4-DOF Magnetic Field Based Localization for UAV Navigation*, Proc. of 2018 International Symposium on Experimental Robotics (ISER), Buenos Aires, Nov. 2018

[9] Mitterer T., Gietler H., Faller L.-M., Zangl H. Artificial Landmarks for Trusted Localization of Autonomous Vehicles Based on Magnetic Sensors. Sensors. 2019; 19(4):813.

[10] Ammari H., Chen J., Chen Z., Garnier J. and Volkov D., "Target detection and characterization from electromagnetic induction data," Journal de Mathématiques Pures et Appliquées, ISSN: 0021-7824, Vol: 101, Issue: 1, Page: 54-75, 2014.

[11] Jackson J.D.: Classical electrodynamics, 3rd ed. edn. Wiley, New York, NY (1999). URL http://cdsweb.cern.ch/record/490457.

[12] Green J. E., Stone D. A., Foster M. P. and Tennant A., "Spatially Resolved Measurements of Magnetic Fields Applied to Current Distribution Problems in Batteries," in IEEE Transactions on Instrumentation and Measurement, vol. 64, no. 4, pp. 951-958, April 2015.

[13] Jaeger H. A. and Cantillon-Murphy P., "Electromagnetic Tracking Using Modular, Tiled Field Generators," in IEEE Transactions on Instrumentation and Measurement.

[14] Wei H. and Wilkinson A. J., "Design of a Sensor Coil and Measurement Electronics for Magnetic Induction Tomography," in IEEE Transactions on Instrumentation and Measurement, vol. 60, no. 12, pp. 3853-3859, Dec. 2011.

[15] Silva A. R. and Moghaddam M., "Design and Implementation of Low-Power and Mid-Range Magnetic-Induction-Based Wireless Underground Sensor Networks," in IEEE Transactions on Instrumentation and Measurement, vol. 65, no. 4, pp. 821-835, April 2016.

[16] Evans L. C., "An Introduction to Stochastic Differential Equations," American Mathematical Soc., 2012

[17] Kuo H.-H., "Introduction to Stochastic Integration," New York, NY: Springer, 2006

[18] Ammari H., Garnier J., Jing W., Kang H., Lim M., Solna K., Wang H., "Mathematical and Statistical Methods for Multistatic Imaging," Lecture Notes in Mathematics, Volume 2098, Springer, Cham, 2013.

[19] Ammari H., Boulier T., Garnier J., Kang H. and Wang H., "Tracking of a Mobile Target Using Generalized Polarization Tensors," SIAM Journal on Imaging Sciences 2013 6:3, 1477-1498.

[20] COMSOL Multiphysics® v.5.2a www.comsol.com. COMSOL AB, Stockholm, Sweden